Analytical and adaptable initial conditions for moist baroclinic waves in a global hydrostatic model

Clément Bouvier[1], Daan van den Broek[1], Madeleine Ekblom[1], and Victoria A. Sinclair[1]

[1]Institute for Atmospheric and Earth System Research/Physics, Faculty of Science, University of Helsinki, Finland

Correspondence: Clément Bouvier (clement.bouvier@helsinki.fi)

Abstract. This article presents a description of an analytical, stable and flexible initial background state for moist baroclinic wave simulation on an aquaplanet in order to test dynamical core of numerical weather prediction models and study the dynamics and evolution of extra-tropical cyclones. The initial background state is derived from an analytical zonal wind speed field, or jet structure, and the hydrostatic primitive equations for moist adiabatic and frictionless flow in spherical coordinates. A baroclinic wave can develop only if a unbalanced perturbation is added to the zonal wind speed field. The implementation of this baroclinic wave simulation have been done on the Open Integrated Forecasting System (OpenIFS) cy43r3, a global numerical weather prediction model developed by the European Centre for Medium-range Weather Forecasts. In total, seven parameters can be used to control the generation of the initial background state and hence the development of the baroclinic waves in the OpenIFS configuration file: the jet's width, the jet's height, the maximum zonal mean wind speed of the jet, the horizontal mean of the surface virtual temperature, the surface relative humidity, the lapse rate and the surface roughness. Nine dry and nine moist initial background states have been generated to test their stability without perturbations. The meteorological stability of the initial state is investigated by examining the spatial distributions of the equivalent potential temperature, the absolute vorticity and the Brunt-Väisälä frequency. Moreover, the Root-Mean-Squared-Error (RMSE) of the zonal wind speed has been computed to assess their numerical stability. Finally, six of these moist initial initial background state have been used with an unbalanced perturbation to ensure that the baroclinic lifecycles developing are physically realistic. The resulting baroclinic wave is shown to be sensitive to the jet's width. This configuration for baroclinic wave simulations will be used to create large baroclinic lifecycles ensemble to study how extra-tropical cyclones may evolve in the future.

1 Introduction

General-Circulation Models (GCMs) are an important tool to predict the extent of global climate change as documented in the IPCC reports (Langsdorf et al., 2022). These GCMs propose numerical solution of the governing equation of the atmosphere. They can take into consideration real-world data to predict the short term evolution of the weather or they can be used to simulate idealised weather system to study specific phenomena of our climate such as convection (Khairoutdinov et al., 2022) or baroclinic waves (Ullrich et al., 2015). Baroclinic waves are the synoptic-scale patterns of high and low pressure systems that develop in the mid-latitudes. These waves develop due to the release of baroclinic instability and the resulting pattern are

25 important parts of the Earth's global circulation as they transport energy polewards (Simmons and Hoskins, 1978; Thorncroft et al., 1993; Beare, 2007).

There exists two main reasons to perform Baroclinic Wave Simulation (BWS). To further improve our weather prediction and climate models, the dynamical cores have to be tested. Most BWS experiments specify a zonally uniform solution to the hydrostatic primitive equations that is statically stable and stable to inertial and symmetric instabilities and then run a numerical

30 model with this specified as the initial state. This type of simulation tests the ability of the numerical model to retain this exact solution in the presence of numerical errors. These initial states are baroclinically and barotropically unstable and therefore adding an unbalanced perturbation triggers the development of a baroclinic wave - to which there is no exact solution (Hoskins and Simmons, 1975; Simmons and Hoskins, 1975; Jablonowski and Williamson, 2006). The baroclinic wave development can be simulated on f-plane or, its extension, β-planes (Feldstein and Held, 1989; Ullrich et al., 2015). These models are often less

35 expensive to run from a computational point of view by simplifying the Coriolis forces. However, these planes require Cartesian geometry, which is a problem to evaluate dynamical cores in a setup close to real-life conditions. Another used approximation alongside f- and β-planes is the restriction of the size of the model where the zonal extent of the domain is roughly equal to the most unstable wavelength (~4000 km) (Hoskins et al., 1977; Ullrich et al., 2015). With this limitation, the dynamical development happens on the top of the main perturbation. This representation can efficiently display the energy propagation

40 of the baroclinic wave. However, it becomes increasingly difficult to study dynamical and synoptic properties without proper display of upstream and downstream developments. Moreover, numerous description and specification of the initial states are available for Cartesian geometry and for channel models (Hoskins et al., 1977; Feldstein and Held, 1989; Wang and Polvani, 2011; Ullrich et al., 2015; Terpstra and Spengler, 2015) and less for spherical geometry and fully global models (Jablonowski and Williamson, 2006), which is one of the main motivation for this work.

45 The Baroclinic Wave Simulations are of interest to study extra-tropical cyclones, extreme cases of which will likely become more frequent in the future (Langsdorf et al., 2022). Extreme cyclones are characterised by strong winds, heavy precipitation and powerful ocean waves. Consequently, these extreme events can damage infrastructure, forests, homes, cause flooding and result in injuries and even death. Depending on the location and the state of the large-scale background environment that the cyclone develops in, the structure and intensity of a given cyclone can vary considerably (Tang et al., 2020). Traditionally, the

50 BWS were adiabatic and the simulations were run without physics (Simmons and Hoskins, 1978; Thorncroft et al., 1993). The main reason being that the synoptic-scale dynamics of baroclinic waves can be largely explained by the classic quasigeostrophic theories of dry baroclinic instability (Charney, 1947; Eady, 1949). Moreover, the latent heat effect on extra-tropical cyclone intensity have been heavily investigated in the last three decades (Kuo et al., 1991; Stoelinga, 1996; Willison et al., 2013; Park et al., 2021). For example, diabatic processes are important to the evolution of the precipitation (Kuo et al., 1991; Park et al.,

55 2021) and smaller-scale systems (Stoelinga, 1996). Moreover, the baroclinic wave sensitivity to moisture and temperature is necessary to be able to predict how cyclones may change in the future, which lead to the development of new BWS in a highly controlled settings using physics (Beare, 2007; Kirshbaum et al., 2018; Tierney et al., 2018; Rantanen et al., 2019).

The sensitivity of the resultant extra-tropical cyclones to the jet structure has been studied (Thorncroft et al., 1993; Shapiro et al., 1999; Rupp and Birner, 2021). Popular jet structures are Z1, Z2 and Z3 resulting in, respectively, LC1, LC2 and LC3

60 baroclinic lifecycles (Thorncroft et al., 1993; Agustí-Panareda et al., 2005). Z2 and Z3 differs from the zonally quasi-symmetric jet of Z1 by respectively including a cyclonic or anti-cyclonic barotropic shear (Thorncroft and Hoskins, 1990; Thorncroft et al., 1993; Shapiro et al., 1999; Polvani and Esler, 2007). Depending on the barotropic shear, baroclinic lifcycles have different structures and intensities (Agustí-Panareda et al., 2005). However, it is difficult to control the height and the width of the jet and test the sensitivity of the BWS to these parameters due to the finite amount of jet structures tested. Here, an initial state

65 is developed, in which the jet's width and vertical structure can be varied in addition to the jet strength. However, setting up a balanced and flexible background state with several jet structures is difficult. The challenges lie in balancing the initial conditions at high resolutions in state-of-the-art models. Few cases are fully documented and can be difficult to reproduce. Many are based on the model developed by Hoskins and Simmons (1975) and rely on numerical integration which is prone to truncation errors. Some are based on Cartesian geometry as presented in Kirshbaum et al. (2018) and their jet are obtained from

70 the potential vorticity inversion method (Heckley and Hoskins, 1982; Olson and Colle, 2007). Having a analytical structure of the jet may allow more control on its structure and strength.

The aim of this study is to describe a balanced, flexible, initial background state for a baroclinic life cycle experiment that can be entirely expressed analytically and that produces relatively realistic weather systems. The analytical solution is derived from a steady-state momentum equation for the meridional wind speed. In other words, the meridional wind speed

75 is constant over time which leads to a gradient-wind balance. Moreover, the proposed background state is also in hydrostatic balance, i.e., the hydrostatic equation was used to derive the virtual temperature anomaly from the geopotential field. The initial background state is also based on a flexibly defined jet structure, and the theoretical description and derivation of the initial state with mathematical formulae is presented in section 2. The technical implementation into the global, state-of-the-art numerical weather prediction model, the Open Integrated Forecasting System (OpenIFS), is described in section 3. The

80 different experiments are described in section 4 and their associated results in section 5. First, the new initial states are run for 15 days with no perturbation to confirm that the initial states are indeed stable both numerically and from a meteorology perspective. Second, six of these moist initial initial background state have been used with an unbalanced perturbation. The evolution of the resulting baroclinic wave that develops from our default initial state are shown.

2   Initial Condition for the Baroclinic Wave

85 This section presents a balanced, steady-state, initial condition for a 3D hydrostatic atmospheric model in spherical coordinates with a flexible jet structure. The moisture field is defined to be consistent with the virtual temperature field. This section describes the theoretical background for the initial conditions and is divided into four parts: (1) analytical derivation of the geopotential and virtual temperature fields, (2) initialisation of moisture, (3) initialisation of the surface (both sea-surface temperature (SST) and roughness), and (4) description of the unbalanced perturbation, which when added triggers the development

90 of the baroclinic wave.

2.1 Analytical Geopotential and Virtual Temperature Fields

The derivation of the analytical initial conditions for geopotential and virtual temperature fields starts from the primitive equations for moist adiabatic and frictionless flow in spherical coordinates and normalised pressure levels. As the geopotential and virtual temperature anomaly fields are derived from hydrostatic equations, the solutions only apply to hydrostatic models.

95 The geopotential and virtual temperature fields are described as the horizontal mean field as a function of vertical levels plus an anomaly field which is a function of longitude, latitude and vertical levels (respectively λ, ϕ, η). The vertical levels are pressure levels normalised with respect to the surface pressure, defined as $\eta = p/p_s$, where p is the pressure on the model level and p_s is the surface pressure. The horizontal means proposed by Ullrich et al. (2015) are used in this background state. The analytical formula of the horizontal mean geopotential is described as

$$100 \quad \langle \Phi(\eta) \rangle = \frac{T_{v,0} g}{\gamma} (1 - \eta^{\frac{R_d \gamma}{g}}) \tag{1}$$

and the horizontal mean virtual temperature field as

$$\langle T_v(\eta) \rangle = T_{v,0} \eta^{\frac{R_d \gamma}{g}}, \tag{2}$$

where γ is the specified lapse rate, $T_{v,0}$ the reference virtual temperature, R_d the gas constant and g the gravity constant. The derivation for the horizontal mean geopotential is available in the Appendix.

105 To be able to derive the anomaly fields of geopotential and virtual temperature, a jet structure has been defined similar to the one proposed by Ullrich and Jablonowski (2012) and Ullrich et al. (2015) with the only difference being the power of the sine function. The power of the sine is described as $2n$ allowing for a narrower jet when n increases. The chosen formula can be expressed as

$$u(\lambda, \phi, \eta) = -u_0 \ln(\eta) \exp[-(\frac{\ln \eta}{b})^2] \sin^{2n}(2\phi), \tag{3}$$

110 where n is a positive integer defining the width of the jet, b is a non-dimensional parameter representing the depth of the jet, and u_0 is the reference zonal wind speed and defines the zonal-mean speed of the jet in the troposphere. As expressed by Eq. (3), the jet width decreases with an increase of n, and the height of the centre of the jet and the vertical width of the jet increase with increasing values of b. The jet reaches its maximum wind speed at $\phi = 45°$ and $\eta(b) = \exp(-\sqrt{b}/2)$. Furthermore, the value for b needs to be positive and smaller than $-\ln(\eta_{top}\sqrt{2})$, where η_{top} is the ratio between the top pressure level and the

115 surface pressure level. For example, a top pressure level of 0.01 hPa and surface pressure level of 1000 hPa, the upper limit for b is about 16. If the value of b exceeds the upper limit, the centre of the jet is located outside the model domain. The analytical geopotential and virtual temperature fields are solved for any jet structure defined by Eq. (3), i.e., for arbitrary values of n and b.

The derivation of the geopotential and virtual temperature anomaly fields start from the primitive equations for moist adi-
120 abatic and frictionless flow (Holton and Hakim, 2012). Following the instructions given in Appendix A of Jablonowski and Williamson (2006), the geopotential anomaly field has been derived from the steady-state momentum equation for the merid-

ional flow ($\partial v/\partial t = 0$) by inserting our choice of jet structure and solving for $\Phi'(\lambda, \phi, \eta)$

$$\frac{1}{a}\frac{\partial \Phi'}{\partial \phi} = -u\left(2\Omega \sin\phi + \frac{u}{a}\tan\phi\right), \tag{4}$$

where Ω is the angular velocity of the Earth, u the jet structure given by Eq. (3), and a the radius of the Earth. A steady-state solution leads to a gradient wind balance, where the centrifugal, Coriolis, and pressure gradient forces are in balance. Integrating Eq. (4) analytically over ϕ results in

$$\Phi'(\lambda, \phi, \eta) = -u_\eta 2a\Omega 4^n \sum_{k=0}^{n}\binom{n}{k}(-1)^k \frac{1}{2(k+n)+1}\cos^{2(k+n)+1}\phi$$

$$-u_\eta^2 16^n \sum_{k=0}^{2n-1}\binom{2n-1}{k}(-1)^k \frac{1}{2(k+2n+1)}\sin^{2(k+2n+1)}2\phi \tag{5}$$

$$+\Phi_0(\eta).$$

Since the deviations of Φ' vanishes when averaging horizontally, Φ_0 is solved by inserting $\Phi'(\lambda, \phi, \eta)$ in the horizontal mean equation

$$\frac{1}{4\pi}\int\limits_{0}^{2\pi}\int\limits_{-\pi/2}^{\pi/2}\Phi'(\lambda, \phi, \eta)\cos\phi d\phi d\lambda = 0, \tag{6}$$

which then give the analytical geopotential anomaly field Φ' as

$$\Phi'(\lambda, \phi, \eta) = u_\eta a\Omega 4^n\left(F_3 - 2F_1\right) + u_\eta^2 16^n\left(\frac{1}{2}F_4 - F_2\right), \tag{7}$$

where

$$F_1 = \sum_{k=0}^{n}\binom{n}{k}(-1)^k \frac{1}{2(k+n)+1}\cos^{2(k+n)+1}\phi, \tag{8a}$$

$$F_2 = \sum_{k=0}^{2n-1}\binom{2n-1}{k}(-1)^k \frac{1}{2(k+2n+1)}\sin^{2(k+2n+1)}2\phi, \tag{8b}$$

$$F_3 = \sum_{k=0}^{n}\binom{n}{k}(-1)^k \frac{1}{2(k+n)+1}\sqrt{\pi}\frac{\Gamma(k+n+3/2)}{\Gamma(k+n+2)}, \tag{8c}$$

$$F_4 = \sum_{k=0}^{2n-1}\binom{2n-1}{k}(-1)^k \frac{1}{2(2n+k+1)}\frac{2}{2(2n+k+1)+1}, \text{ and} \tag{8d}$$

$$u_\eta = u_0 \ln\eta \exp(-[\ln\eta/b]^2). \tag{8e}$$

Note that $\binom{n}{k}$ is the binomial coefficient representing the k unordered outcomes from n possibilities, $\Gamma(x)$ is the Gamma function for positive half-integer $x = z + 1/2$ with z a positive integer, and $2n$ is the power of the sine in the jet structure.

The total geopotential field is described as the sum of the mean horizontal geopotential field and the anomaly geopotential field as

$$\Phi(\lambda, \phi, \eta) = \frac{T_{v,0}g}{\gamma}(1 - \eta^{\frac{R_d\gamma}{g}}) + u_\eta a\Omega 4^n\left(F_3 - 2F_1\right) + u_\eta^2 16^n\left(\frac{1}{2}F_4 - F_2\right). \tag{9}$$

The virtual temperature anomaly field is then derived by inserting $\Phi'(\lambda,\phi,\eta)$ into the hydrostatic equation and taking the derivative of Φ' with respect to η

$$T_v'(\lambda,\phi,\eta) = -\frac{\eta}{R_d}\frac{\partial\Phi'(\lambda,\phi,\eta)}{\partial\eta}, \tag{10}$$

which gives the virtual temperature field

150 $T_v(\lambda,\phi,\eta) = \langle T_v(\eta)\rangle + T_v'(\lambda,\phi,\eta)$

$$= T_{v,0}\eta^{\frac{R_d\gamma}{g}} + \frac{u_0}{R_d}\exp[-(\ln\eta/b)^2]\left[\frac{2(\ln\eta)^2}{b^2}-1\right]\left[a\Omega 4^n\left(F_3-2F_1\right)+16^n u_\eta\left(F_4-2F_2\right)\right], \tag{11}$$

where F_1, F_2, F_3, F_4 and u_η are as defined in Eq. (8). A detailed step-by-step derivation of the analytical geopotential and temperature anomaly fields is available in Appendix A.

2.2 Moisture Initialisation

155 As stated in the Introduction, the proposed background state can be used in dry and moist cases studies. In order to set the latter, a relative humidity profile with respect to water $RH(\eta)$, depending on the model level η and the surface relative humidity RH_0, has been defined. It is inspired from the ERA-Interim (Romps, 2014) and ERA5 (Gamage et al., 2020) average relative humidity profile. The profile, as shown in Figure 1, has a maximum value of the RH_0 at the surface, above which it decreases to 70 % RH_0 at 800hPa. Between 800 and 300hPa RH is constant and above 300 hPa it again decreases linearly to 0 at 100

160 hPa. Above 100 hPa RH is set to zero. The profile is given as

$$RH(\eta) = \begin{cases} 0.0 & \text{between 0 and 100 hPa} \\ (3.5\eta - 0.35)RH_0 & \text{between 100 and 300 hPa} \\ 0.7RH_0 & \text{between 300 and 800 hPa} \\ (1.5\eta - 0.5)RH_0 & \text{between 800 and 1000 hPa.} \end{cases} \tag{12}$$

The specific humidity field $q(\lambda,\phi,\eta)$ is then computed to ensure concordance with the proposed virtual temperature and jet structure. It is derived from the relative humidity $(RH(\eta))$, the saturation vapour pressure (e_s) and the saturation mixing ratio

165 (w_s) as presented in the following equations (Yau and Rogers, 1996).

$$e_s(\lambda,\phi,\eta) = 611.21\exp\frac{17.67(T_v(\lambda,\phi,\eta)-273.15)}{T_v(\lambda,\phi,\eta)-29.65}, \tag{13a}$$

$$w_s(\lambda,\phi,\eta) = \frac{0.622e_s(\lambda,\phi,\eta)}{p-e_s(\lambda,\phi,\eta)} \text{ with p the pressure.} \tag{13b}$$

Finally, $w_s(\lambda,\phi,\eta)$ and $RH(\eta)$ are used to infer $q(\lambda,\phi,\eta)$ as

$$q(\lambda,\phi,\eta) = \frac{w_s(\lambda,\phi,\eta)RH(\eta)}{w_s(\lambda,\phi,\eta)RH(\eta)+100}. \tag{14}$$
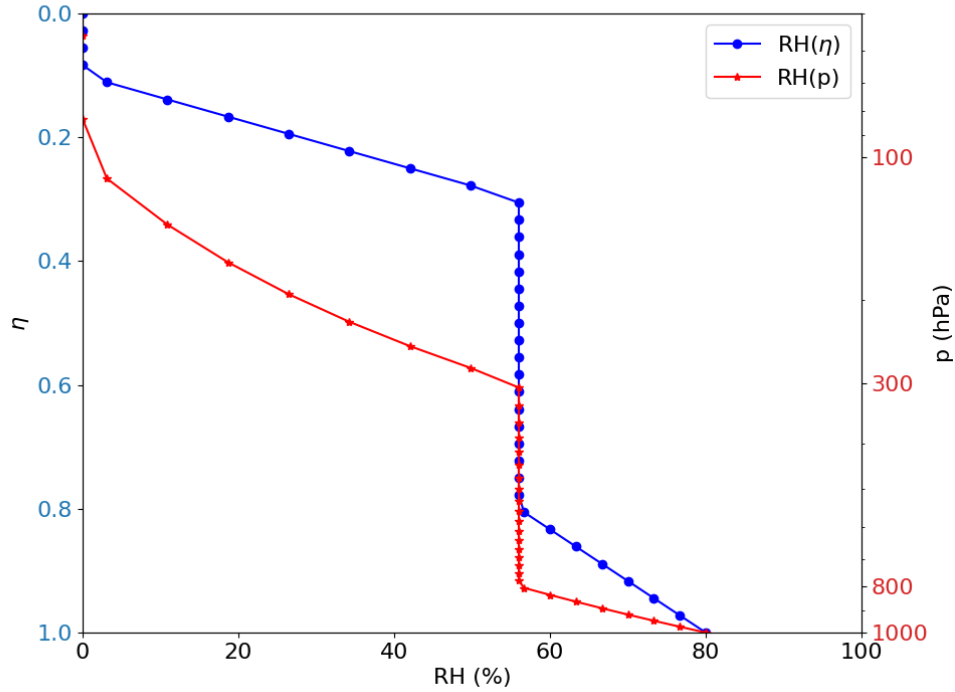
Figure 1. Relative humidity profile for $RH_0 = 80\%$. The blue curve is the profile against normalised pressure levels, η, and the red one against pressure, p, in logarithmic scale.

The formulation of the virtual temperature and specific humidity leads to the following expression

$$T(\lambda, \phi, \eta) = \frac{T_v(\lambda, \phi, \eta)}{1 + 0.608 q(\lambda, \phi, \eta)}. \tag{15}$$

2.3 Surface Initialisation: Temperature and Roughness

A uniform sea surface with no land has been chosen for the described background state. Thus, the experiments presented here were conducted using an aquaplanet setting which is the traditional configuration of baroclinic wave simulation (Jablonowski and Williamson, 2006; Ullrich et al., 2015). The Sea Surface Temperature (SST) is zonally uniform and is specified to equal the temperature field at $\eta = 1$ (see Eq. (15)), which means negative temperatures are allowed. If the SST differed from the near surface atmospheric temperature, then in the moist cases there would be non-zero surface sensible heat fluxes which could either heat or cool the boundary layer. Such fluxes could trigger convection, destabilising the proposed background state. The proposed SST is stated as

$$T_{SST}(\lambda, \phi, \eta) = \frac{T_{v,0} - \frac{u_0 a \Omega}{R_d} 4^n \left(F_3 - 2F_1\right)}{1 + 0.608 q(\lambda, \phi, \eta = 1)}, \tag{16}$$

7

where F_1 and F_3 are described in Eq. (8).

To complete the surface initialisation, the Charnock parameter is specified to control the surface roughness (Charnock, 1955). The surface roughness lengths for momentum (M), heat (H), and total water (Q) air-surface transfers are defined in OpenIFS (Eq. 3.26 ECMWF, 2017b) (and (Eq. 25 Beljaars, 1995)). OpenIFS will be described in the next section.

$$z_{0M} = \alpha_M \frac{\nu}{u_\star} + \alpha_{Ch} \frac{u_*^2}{g} \tag{17a}$$

$$z_{0H} = \alpha_H \frac{\nu}{u_\star} \tag{17b}$$

$$z_{0Q} = \alpha_Q \frac{\nu}{u_\star}, \tag{17c}$$

where α_{Ch} is the Charnock parameter, $u_\star$ the friction velocity, ν kinematic viscosity, and α_M, α_H and α_Q are constants set 0.11, 0.40 and 0.62, respectively. Being able to tune the Charnock parameter allows the modification of the surface friction which previous studies have shown to influence the intensity of extra-tropical cyclones (Adamson et al., 2006; Sinclair et al., 2010) and the structure of warm and cold fronts (Hines and Mechoso, 1993; Sinclair and Keyser, 2015). in case of high wind speed regimes which is the regime of baroclinic wave simulations.

2.4 Initial Perturbation

The baroclinic wave can be triggered by adding a localised unbalanced wind perturbation to a baroclinically unstable background state as the one described in Section 2.1. A Gaussian perturbation was chosen and it was centred at $(\lambda_c, \phi_c) = (\frac{\pi}{9}, \frac{2\pi}{9})$ which corresponds to 40° N, 20° E (Jablonowski and Williamson, 2006; Ullrich et al., 2015). The equation of the perturbation is given by

$$u_\epsilon(\lambda, \phi, \eta) = u_p \exp[-(\frac{r}{R})^2], \tag{18}$$

where $R = \frac{a}{10}$, $u_p = 10$ ms^{-1} and r the great circle distance given by

$$r = a \arccos(\sin\phi_c \sin\phi + \cos\phi_c \cos\phi \cos(\lambda - \lambda_c)). \tag{19}$$

The final zonal wind field is obtained by adding u_ϵ to u at each grid point at all model levels

$$u_{total}(\lambda, \phi, \eta) = u(\lambda, \phi, \eta) + u_\epsilon(\lambda, \phi, \eta). \tag{20}$$

3 Implementation into OpenIFS

3.1 OpenIFS

The proposed background state has been implemented in the Open Integrated Forecasting System (OpenIFS) cycle 43r3v2 which is based on the Integrated Forecasting System of the European Centre for Medium-range Weather Forecasts (ECMWF) cycle 43r3, which was operational from July 2017 to June 2018 (ECMWF (2017a)). OpenIFS is a version of the Integrated

Forecasting System model but does not include data assimilation capacities. Despite its name, OpenIFS is not open source but available to universities and research institutions under license. The model is hydrostatic, spectral and has the same physical

210   parameterization schemes as the full version of the IFS. In terms of applications, OpenIFS is able to compute deterministic and ensemble forecasts from either real, specified or idealised initial conditions. The project is coded in FORTRAN and in C, which is efficient for intensive and scientific computing.

3.2   Existing implementation

In OpenIFS version 43r3v2, the idealised background state implemented for the baroclinic wave test case is the one developed

215   by Jablonowski and Williamson (2006). Originally, this background state was implemented in the full version of the IFS, and hence OpenIFS, to test the dynamical core. Therefore, this test case had only been run on an idealised aquaplanet in the dry case with no physics, no radiation scheme, and no wave model. The original initial state of Jablonowski and Williamson (2006) has a very strong meridional temperature gradient which means that the near-surface temperature reaches -50°C at high latitudes. On an aquaplanet, the SSTs need to be specified everywhere as there is no sea ice. For a physically meaningful

220   configuration, the minimum SSTs should not be below the freezing point of salt water (-1.8C). In the dry case with no physics, the surface heat fluxes are not computed meaning that the SSTs can be specified to be much warmer (or colder) than the near-surface atmospheric temperatures without causing any problems such as destabilisation of the boundary layer or convection. In contrast, in the moist case with physics on an aquaplanet, exceptionally cold conditions at high latitudes with physically realistic SSTs below cause large surface heat fluxes to develop and in the extreme case can result in low pressure centres resembling

225   polar lows developing at high latitudes. Therefore, modifications to the Jablonowski and Williamson (2006) case are needed to enable it to be run with physics and to allow it to be used to investigate cyclone dynamics rather than the numerical accuracy of dynamical cores. Lastly, many aspects of the existing implementation are hard coded, and the parameters used to compute the background state were not accessible via the OpenIFS namelist.

3.3   The new implementation: OpenIFS baroclinic wave v1.0

230   The proposed background state is implemented into OpenIFS based on the derived analytical equations for the geopotential and temperature field as detailed in Section 2. Both fields contain complex functions - such as the Gamma function (see Eq. (8)) - and can be difficult to implement. In order to avoid the costly use of factorials, F_3 was expressed as a binomial coefficient fraction and all the binomial coefficients were computed once with the multiplicative method, since $\binom{z}{k+1} = \frac{z-k}{k+1}\binom{z}{k}$ with z, k integers. By using the definition for the gamma function for positive integers z

235    $$\Gamma(z) = (z-1)! \text{ and } \Gamma(z+1/2) = \frac{(2z)!}{4^z z!}\sqrt{\pi}, \tag{21}$$

the factorials can be removed from F_3 as follows

$$\frac{\Gamma(k+n+3/2)}{\Gamma(k+n+2)} = \frac{\Gamma(k+n+1+1/2)}{\Gamma(k+n+1+1)}$$

$$= \frac{\Gamma(z+1/2)}{\Gamma(z+1)} \text{ where } z = k+n+1$$

$$= \frac{(2z)!}{4^z z!}\sqrt{\pi}\frac{1}{z!} \text{ Note: } \binom{2z}{z} = \frac{(2z)!}{z!z!}$$

$$= \binom{2z}{z}\frac{\sqrt{\pi}}{4^z}$$

$$= \binom{2(k+n)+2}{k+n+1}\frac{\sqrt{\pi}}{4^{k+n+1}}.$$

F_3 can then be rewritten as

$$F_3 = \sum_{k=0}^{n}\binom{n}{k}(-1)^k\frac{1}{2(k+n)+1}\binom{2(k+n)+2}{k+n+1}\frac{\pi}{4^{k+n+1}}. \tag{22}$$

The proposed solution has been implemented as a new idealised case (indicated by the NTESTCASE parameter in OpenIFS) alongside the solution of Jablonowski. The proposed background state is set on an idealised aquaplanet with most of the physics of OpenIFS switch on but no radiation scheme and no wave model. The customised SST function presented in Eq. (16) has been added to the other SST schemes already implemented in OpenIFS and is identified with the number 10 in the NAEPHY namespace (variable name MSSTSCHEME in OpenIFS). In the OpenIFS namelist, the NAMDYNCORE and NAEPHY are important namespace to fill in order to ensure the correct configuration and set up of the baroclinic wave simulation. The NAMDYNCORE namespace sets up all of the idealised model configurations and NAEPHY the different physical parametrisation schemes (i.e. whether they are activated or not). Finally, the NAMCT0 namespace set the main model control variables. N3DINI was set to 3 meaning that the meteorological values in the initial grib files were ignored and replaced by the idealised background state. The default values for the simulation in the moist case are presented in Table 1.

3.4 How to use the new implementation?

Subsequent baroclinic wave simulations were run in the dry and moist case. The difference between the dry and moist case is the computation of virtual temperature (see Eq. (15)) and a non-zero specific humidity. In the dry case, the computation of specific humidity is disabled and thus the virtual temperature is equal to the real temperature at all time. The dry and moist test case can be computed by setting the NTESTCASE value to 41 or 42 respectively. The current solution allows the user to switch on or off the perturbation specified in Section 2.4. Moreover, the user can define the amplitude of the Gaussian hill by changing the value of ZUP in the namelist. It would be possible to use a perturbation with a different structure, but that would require the user to modify the source code. In total, six parameters were input to create various different background states and influenced the resulting baroclinic wave, one controlled the surface roughness (α_{Ch}) and and one triggered the initial perturbation (u_p). All parameters were included in the NAMDIM namespace in the OpenIFS namelist. A default case was defined as shown in Table 2. Of these parameters, only ZCHAR and ZUP are not used to compute the initial background state.

Table 1. Template of the namelist used to set the proposed background state in the moist case. All other parameters under NAEPHY were set to false.

Field	Parameter	Value
NAMCT0	N3DINI	2
NAMDYNCORE	LAPE	true
	LAQUA	true
	MSSTSCHEME	10
	NTESTCASE	42
NAEPHY	LEPHYS	true
	LEVDIF	true
	LESURF	true
	LECOND	true
	LECUMF	true
	LEPCLD	true
	LEEVAP	true
	LEQNGT	true
	LERADI	false
	LERADS	false

Table 2. Modifiable parameters with their default values and short description with units in NAMDIM namespace

Parameter	Default value	OpenIFS given name	Function
n	3	ZN	Jet width
b	2.0	ZB	Jet height
u_0	35.0	ZU0	Maximum zonal mean wind speed (ms^{-1})
$T_{v,0}$	288.0	ZT0	Average surface virtual temperature (K)
RH_0	80.0	ZRH0	Surface level relative humidity (%)
γ	0.005	ZGAMMA	Lapse rate (Kkm^{-1})
α_{Ch}	0.013	ZCHAR	Charnock value
u_p	1.0	ZUP	Initial wind speed of the perturbation (ms^{-1})

265   In Section 5, the "dry case" case refers to the dry simulations without physics and the "moist case" case is describing the case with physics and with moisture included.

4   Description of the experiments and diagnostics

This section is divided into three parts: (1) numerical stability of the initial background state (dry case and moist case), (2) meteorological stability and structure of the initial states (3) evolution of the baroclinic waves for different initial background
270   states. All simulation are run at T_L319 L137 resolution (i.e., 63km horizontal resolution at the equator), with a timestep of 900 seconds for 15 days with an output frequency of 3 hours. Simulations without the perturbation were conducted to test the stability of the proposed background state: if implemented correctly and numerical errors are small, the initial state should not change in time. The jet width and height were varied by changing n and b, and all other parameters presented in Table 2 were set to their default value. In total, 18 background states without the unbalanced wind perturbation were tested for 3 values of n
275   (1, 3, 6), 3 values of b (1, 1.5, 2) and for both the dry and moist cases.

    The Root-Mean-Square-Error (RMSE) is computed across all vertical levels for the zonal wind (Eq. 4.2, Jablonowski and Williamson, 2006) and also shown in Eq. 23.

$$RMSE(u_{za}(t) - u_{za}(t=0)) \approx \left(\frac{\sum_{\eta_i=\eta_{surface}}^{\eta_{top}} \sum_{\phi_j=-90°}^{90°} [u_{za}(\phi_j,\eta_i,t) - u_{za}(\phi_j,\eta_i,t=0)]^2 w_{\phi_j} \Delta\eta_i}{\sum_{\eta_i=\eta_{surface}}^{\eta_{top}} \sum_{\phi_j=-90°}^{90°} w_{\phi_j} \Delta\eta_i} \right)^{\frac{1}{2}} \quad (23)$$

where u_{za} is the zonal average of the zonal wind speed, w_{ϕ_j} is the location of the cell interfaces in the meridional direction ϕ_j
280   and $\Delta\eta_i$ is the thickness of the model layer η_i.

    Previous studies have used several metrics to test the meteorological stability of their background states such as the temperature, geopotential height, and zonal winds (Khairoutdinov et al., 2022), sometimes potential temperature, absolute vorticity and the Brunt-Väisälä frequency are added (Jablonowski and Williamson, 2006; Ullrich et al., 2015). The absolute vorticity, potential temperature, equivalent potential temperature, zonal wind, Brunt-Väisälä frequency were computed to test if the initial
285   state is stable to static (gravitational), inertial, and symmetric instability. For the initial state to be absolutely stable to vertical displacements (static stability), equivalent potential temperature must increase with height everywhere. In the situation where equivalent potential temperature decreases with height, conditional instability is present, meaning that the atmosphere is stable to displacements of dry and unsaturated air parcels but unstable to displacements of saturated air parcels. If potential temperature decreases with height, then the atmosphere is absolutely unstable - both dry and saturated displacements are unstable.
290   Thus, for the initial state to be absolutely stable potential temperature must increases with height and the Brunt-Väisälä frequency must be positive. For the initial state to be stable to horizontal displacements (inertial stability) the absolute geostrophic vorticity must be positive (negative) in the northern (southern) hemisphere. Situations can exist where the atmosphere is statically and inertially stable, but the atmosphere is unstable to slantwise displacements (symmetric instability). This exists when the geostrophic potential vorticity is negative. Hence for our initial state to be stable to inertial and symmetric instability, both
295   the absolute geostrophic vorticity and geostrophic potential vorticity must be positive in the northern hemisphere. However,

although the initial state must be stable to static, inertial and symmetric stability, must be baroclinically unstable. This requires there to be a meridional temperature gradient in the mid-latitudes and a well defined zonal jet.

Several baroclinic waves (background states with perturbation) are generated for 6 values of n (1 to 6) and the default values for the remaining parameters (presented in Table 2). All BWS have been run for 15 days. During the 15 day simulation, the first

300 cyclone to emerge develops directly from the initial perturbation, however, upstream and downstream development also occurs resulting in multiple cyclones and anticyclones. To objectively identify the centre of the cyclone which develops directly from the initial perturbation (the first cyclone) the TRACK software (Hodges, 1994, 1995, 1999) is used. Cyclones are identified as localised maxima in the 850-hPa relative vorticity field truncated to T42 spectral resolution. Only tracks lasting for 4 days and which travel 1000 km are retained. The weak tracks are removed by setting a threshold of $0.4 \times 10^{-5} \mathrm{s}^{-1}$ on the T42 850-hPa

305 relative vorticity. This threshold is weaker that the threshold usually applied when using TRACK ($1 \times 10^{-5} \mathrm{s}^{-1}$) to identify cyclones in the real world to enable to first cyclone to be detected as soon as possible.

5 Results

5.1 Numerical stability of the initial background state

As shown in Figure 2, the RMSE for all of the dry cases with no perturbation included oscillate below $0.1 \mathrm{~ms}^{-1}$ with no

310 noticeable increase over time. These values are lower than the RMSE in the Jablonowski and Williamson (2006) report for the same semi-Lagrangian setup and comparable with the one reported in the Khairoutdinov et al. (2022) study. This means that the specified background states are stable and correctly implemented into OpenIFS. A similar tendency is observed for the moist cases with the exception of the n=1 b=1 case (called n1b1 in the rest of this article), which will be investigated in the next section. The RMSE are nearly identical between the dry and moist cases. The lower the n value and the higher the b value,

315 the higher the RMSE. This tendency can be understood as more extensive the jet is, the higher the RMSE. The amplitude of the oscillations have the tendency to increase with the average RMSE, which can be linked with the fact that the wind speed is output as spectral harmonics. A possible explanation is the error of interpolation during the computation of advection of the zonal wind in the semi-Lagrangian setup. This error of interpolation is documented in chapter 3 of ECMWF (2017a) and in previous studies (Purser and Leslie, 1988; Ritchie and Beaudoin, 1994). Another explanation is the de-aliasing procedure

320 applied in OpenIFS in the conversion to regular grids (see page 16 in ECMWF (2017a) and Courtier and Naughton (1994)).

5.2 Meteorological stability and structure of the initial background state

The initial fields for the default values (n=3 and b=2.0) in the moist case are presented in Figure 3. A strong baroclinic zone is present between 30 and 60 degrees (Figure 3 a, b and Figure 4 d) with temperatures at the surface reaching a maximum of 23.0°C at the equator and decreasing to -13.0°C at the poles. These temperatures are similar to the temperatures reported in the

325 ERA5 global re-analysis, which display a surface temperature between 20°C and 30°C in the tropics and between -10°C and -20°C at the poles (Hersbach et al., 2020). The baroclinic zone is co-located with a jet stream between 20°N/S and 70°N/S with
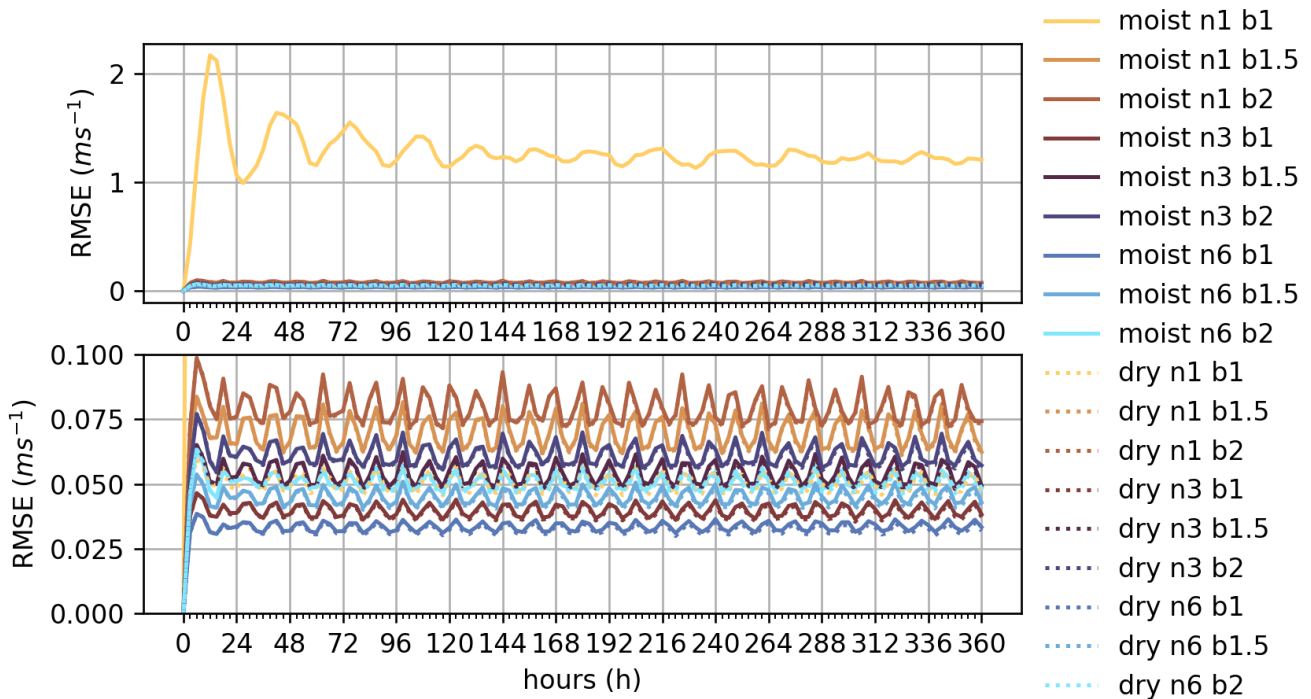
Figure 2. RMSE for all cases. The solid lines represents the moist cases and the doted lines the dry cases. The upper panel scales the RMSE between 0.0 and 2.2 ms^{-1}, the lower panel constraint the y-axis between 0.0 and 0.1 ms^{-1}. Hues represent cases by n values and colour value by b values: the green hues represent n=1, the blue hues n=3 and the red hues n=6.

a maximum zonal wind speed of 30 ms^{-1} located in the centre of the jet at 45N/S and 250 hPa as shown in Figure 3 c. When the width and height of the idealised jet streams that we propose in this study are compared to realistic values from ERA5 (see Lee et al. (2023)), reasonable agreement is found for winter means over the northwestern atlantic. However, the maximum
330   zonal wind speed is on the lower range of the maximum wind speed of ERA5 profile, which is not a problem considering that u_0 is a tunable parameter as presented in Table 2. Moreover, the December mean zonal wind speed over the years 1979 - 2021 was computed (Figure S1) and compared it to our idealised jet structures (Figure S2). A 10° location difference of the centre of the northern jet have been found but the proposed analytical solution is close in shape and intensity to this profile. The potential temperature (Figure 3 a) increases with height everywhere in the model domain indicating that the initial state is stable to dry
335   static stability. Figure 3 b shows that the equivalent potential temperature increases everywhere, except for the tropical regions. This means that the initial state is stable to moist static stability, as long as air parcels are not saturated in the tropics. The static stability is also indicated by the Brunt-Väisälä frequency presented in (Figure 3 d). Relatively high values for the Brunt-Väisälä frequency were seen at high latitudes at most pressure levels, indicating high static stability. A lower Brunt-Väisälä frequency and thus lower static stability was observed around the equator and near the surface in the polar regions. The absolute vorticity,

340 presented in Figure 3 e, demonstrates that the default initial state is inertially stable. The condition for symmetric stability, that geostrophic potential vorticity is positive in the northern hemisphere and negative in the southern hemisphere, is also met. This can be inferred from the potential temperature distribution (Figure 3 a) combined with the absolute vorticity distribution (Figure 3 e).
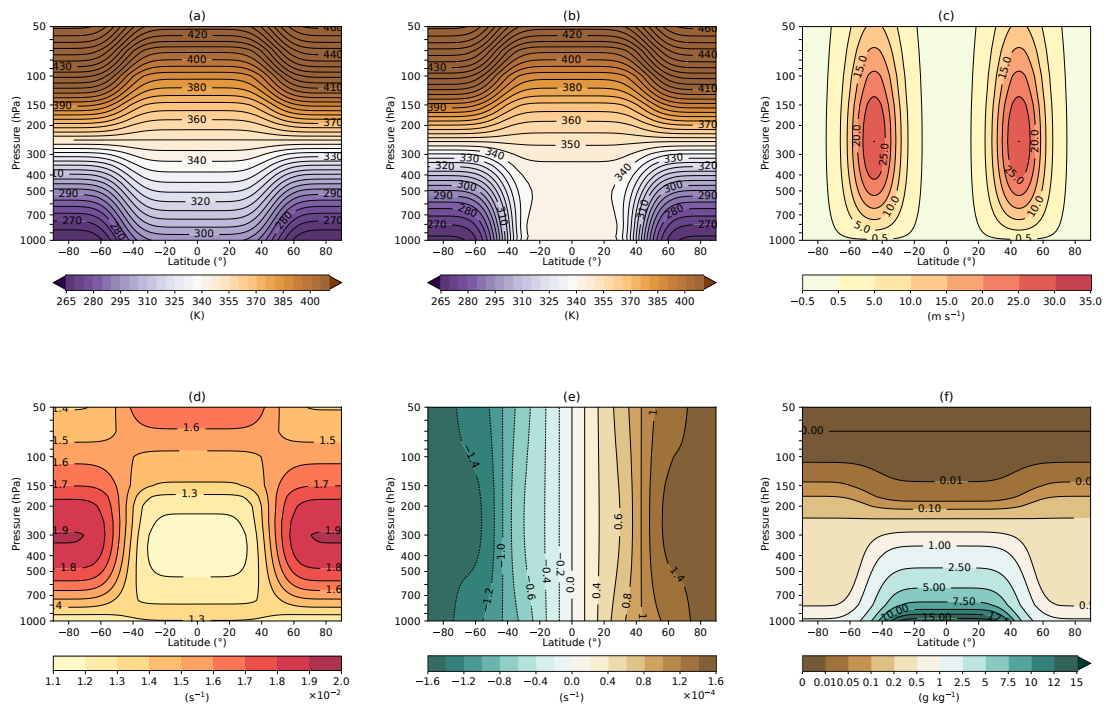

Figure 3. Cross sections of the default initial background state (n=3 and b=2.0) for: (a) potential temperature, (b) equivalent potential temperature, (c) wind speed, (d) Brunt-Väisälä frequency, (e) absolute vorticity and (f) specific humidity.

Figure 4 shows the initial temperature, zonal wind speed and dynamical tropopause (taken here to be the 2 PVU surface)for

345 different values of n (1, 3 and 6) and b (1, 1.5 and 2), with Fig. 4d showing the default initial state which was presented in Fig. 3. Increasing n causes the meridional width of the jet to decrease. In the case of n =1, the jet is very wide extending from 15°N/S to 75°N/S. In contrast, when n =6, the jet is constrained between 30 and 60°N/S. Increasing n also causes the width of the baroclinic zone to decrease and the surface temperature gradient between the equator and pole to decrease: in the case of n =1, the temperature difference between the equator and pole is 56.6°C whereas for n =6 the temperature difference is

350 21.1°C. Decreasing b leads to the displacement of the centre of the jet toward the surface. For all initial states, higher values for

n lead to a narrower jet and a stronger temperature gradient (Figure 4). Moreover, high values of b lead to stronger temperature gradient, higher centre of the jet and an increase of the maximum wind speed of the jet as shown by the innermost contour (e.g. Figure 4 a and c). Additionally, the centre of the jet gets closer to the surface with b decreasing. For $b=1$, the centre of the jet is lower than the dynamical tropopause at 2 PVU. The latitudinal location of the centre of the jet is independent of n and b and located at $45°$ in both hemispheres for all the different initial cases presented. The height of the dynamical tropopause increase with n increasing, which means that the static stability increase with higher n (Held, 1982).
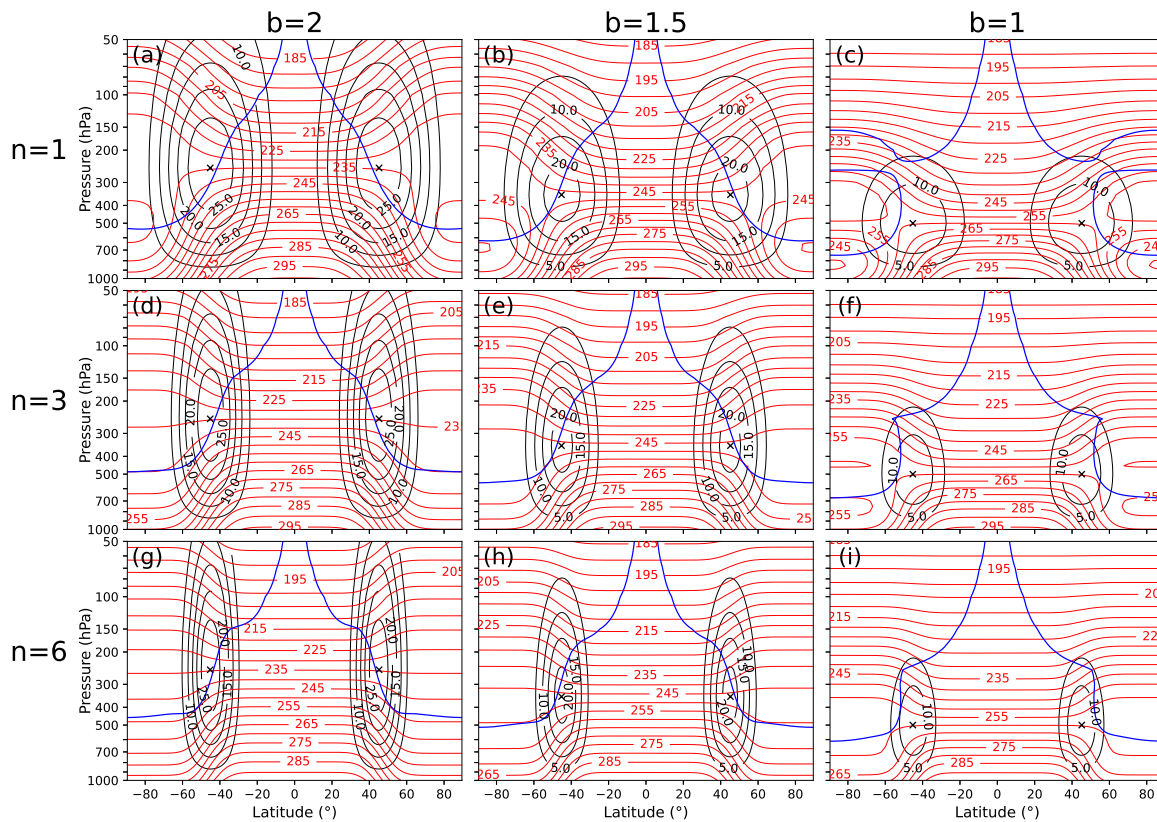
Figure 4. The zonal wind speed in ms^{-1} (black contours), temperature in K (red contours) and dynamical tropopause at 2 PVU (blue contours) fields of the initial state for different values of n and b.

As noted in section 5.1, the moist case n1b1 can be considered as an outlier compared to the other cases. As shown Figure 2, its RMSE oscillates around 1.25 ms^{-1}. The amplitudes of the oscillation reduce over time from 75% of the asymptotic limit to less than 4%. No global increase over time can be noticed. This exception can be explained by an exceptionally strong

360 temperature gradient in the tropics as shown in Figure 4 c. This produces substantial convective available potential energy (CAPE) in the tropics and under the dynamical tropopause as shown in the Supplementary material (Figure S3). On a general note, $n=1$ is does not resemble a realistic jet structure as found in reanalysis (Lee et al., 2023) and the average zonal wind speed profile between 1979 and 2021 produced for the Supplementary material (Figure S1 and S2), which makes the width improper to study extra-tropical cyclone dynamics.

365 As the main instability is located in the tropics and the RMSE stabilises over time, it is unlikely that this instability will influence the development of baroclinic wave in the mid-latitudes. Based on the results of the previous and the current Section, the initial background states can be considered as stable through time and balanced on a meteorological perspective. As shown in Figure 4, the background states display a strong baroclinicity in the mid-latitudes. The next Section will present the evolution of the baroclinic waves triggered in some of the presented background states (b=2.0).

370 ## 5.3   Evolution of the baroclinic wave for different initial background states

The evolution of the default baroclinic wave (n=3, b=2) with moisture is shown in Figure 5. The formation of a closed low pressure system is evident after 144 h (Figure 5a). At this time, the minimum MSLP is located slightly poleward of 45°N which was the central latitude of the initial perturbation. Also at 144 h, a small amplitude wave in the 850-hPa temperature is evident co-located with the developing cyclonic circulation but pronounced fronts have not yet developed. After 168 h of
375 development (Figure 5b), the cyclone has a minimum MSLP of approximately 994 hPa. Two areas of high pressure are evident on either side of this cyclone and another cyclone has begun developing upstream of the cyclone which developed directly from the initial unbalanced perturbation. By 192 h, (Figure 5c) a well developed cyclone is present with a minimum MSLP below 990 hPa. Cold and warm fronts are now evident in the 850-hPa temperature. The centre of the cyclone has continued to move polewards and the two anticyclones on either side have also intensified slightly and moved equatorwards. In addition
380 to the upstream development that was evident 24 h previously, downstream development has also started to take place by 192 h; a third low pressure centre / cyclone is now visible at 150°E although this is the weakest of all three cyclones. Rapid intensification takes place and by 228 h (Figure 5d), the initial cyclone has deepened considerably (minimum MSLP below 978 hPa). Cold and warm fronts with large thermal gradients are present and an occlusion has begun to develop. Furthermore at 228 h, both the upstream and downstream cyclones have continued deepening, with the upstream cyclone being deeper yet
385 spatially smaller than the downstream cyclone. By 264 h (Figure 5e), the initial cyclone is very mature, deep, and has moved farther polewards. The downstream cyclone has undergone notable deepening since 228 h and a fourth cyclone has started to develop upstream. After 312 h of simulation, three of the four cyclones are very mature systems and the three anticyclones are also well developed and have moved equatorward. Overall, Figure 5 demonstrates that the cyclones and anticyclones that develop from the default initial state are realistic and consequently can be used to investigate cyclone dynamics. In comparison
390 to previous BWS studies that have used limited model domains with periodic boundaries (Feldstein and Held, 1989; Hoskins et al., 1977), the set up presented here and the evolution of the default baroclinic wave allow for studies into both upstream and downstream development.

Figure 6 demonstrates how the structure of the baroclinic wave depends on the value of n after 204 h. Decreasing n increases the width of the jet stream and the baroclinic zone (Fig. 4) which means that the resultant cyclones have a greater meridional

395　extent with smaller values of n. Decreasing n leads to a reduction in the minimum surface pressure of the cyclones: for n=1, the minimum surface pressure of the first developing cyclone after 204 h is 978 hPa (Fig. 6a) whereas for n=6 the corresponding value is 988 hPa (Fig. 6f). This also holds true for the cyclones which develop upstream and downstream and is likely because the 850-hPa temperature difference between the equator and the pole, and hence available potential energy and baroclinicity, is larger with smaller n (Fig. 6). Decreasing n also causes the phase speed of the cyclones to increase and the cyclones and

400　anticyclones travel eastward faster with larger n, despite that the maximum speed of the zonal jet does not change considerably. A detailed investigation of how all parameters which control the structure of the initial state (as presented in Table 2) affect the intensity and structure of the resultant cyclones will be the topic of a future study.

Figure 7 shows the temporal evolution of the maximum 850-hPa relative vorticity as identified by TRACK of the cyclone which develops first in experiments with different n. Note that this is not necessarily the cyclone which experiences the largest

405　deepening rates nor the largest maximum vorticity but it is the cyclone which is directly caused by the initial unbalanced perturbation. The first cyclone in all experiments is detected by TRACK after 5 – 6 days. Between day 7 and day 10, a period of rapid intensification occurs for all experiments. The maximum relative vorticity is reached after 10.5 days (264 hours) of simulation for all experimental set-ups after which there is a gradual weakening in the maximum vorticity. As n decreases, the rate of intensification increases particularly between day 8 and day 10, and the eventual maximum value of relative vorticity

410　is larger for smaller n. This is consistent with Fig. 6 which showed that the minimum surface pressure was also lower with smaller n and that the 850-hPa temperature difference between the poles and the equator was larger with smaller n.
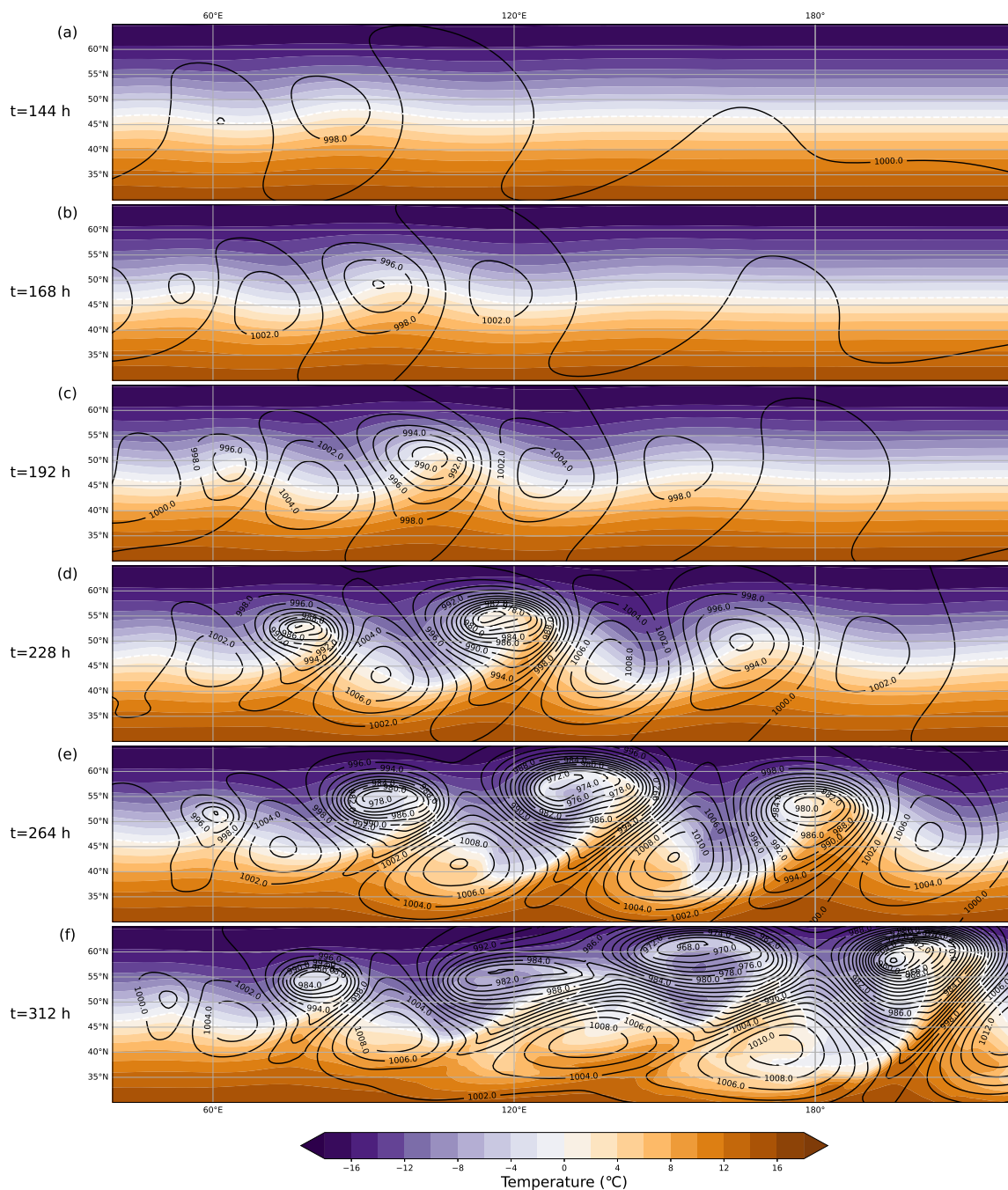
Figure 5. The development of the baroclinic wave for the default scenario at (a) t=144 h, (b) t=168 h, (c) t=192 h, (d) t=228 h, (e) t=264 h, (f) t=312 h. The black contours show mean sea level pressure (hPa), the shading shows the temperature (°C) at 850 hPa. Note: this figure does not show the whole model domain; the x-axis ranges from 40-220°E, while the y-axis ranges from 30-65°N.
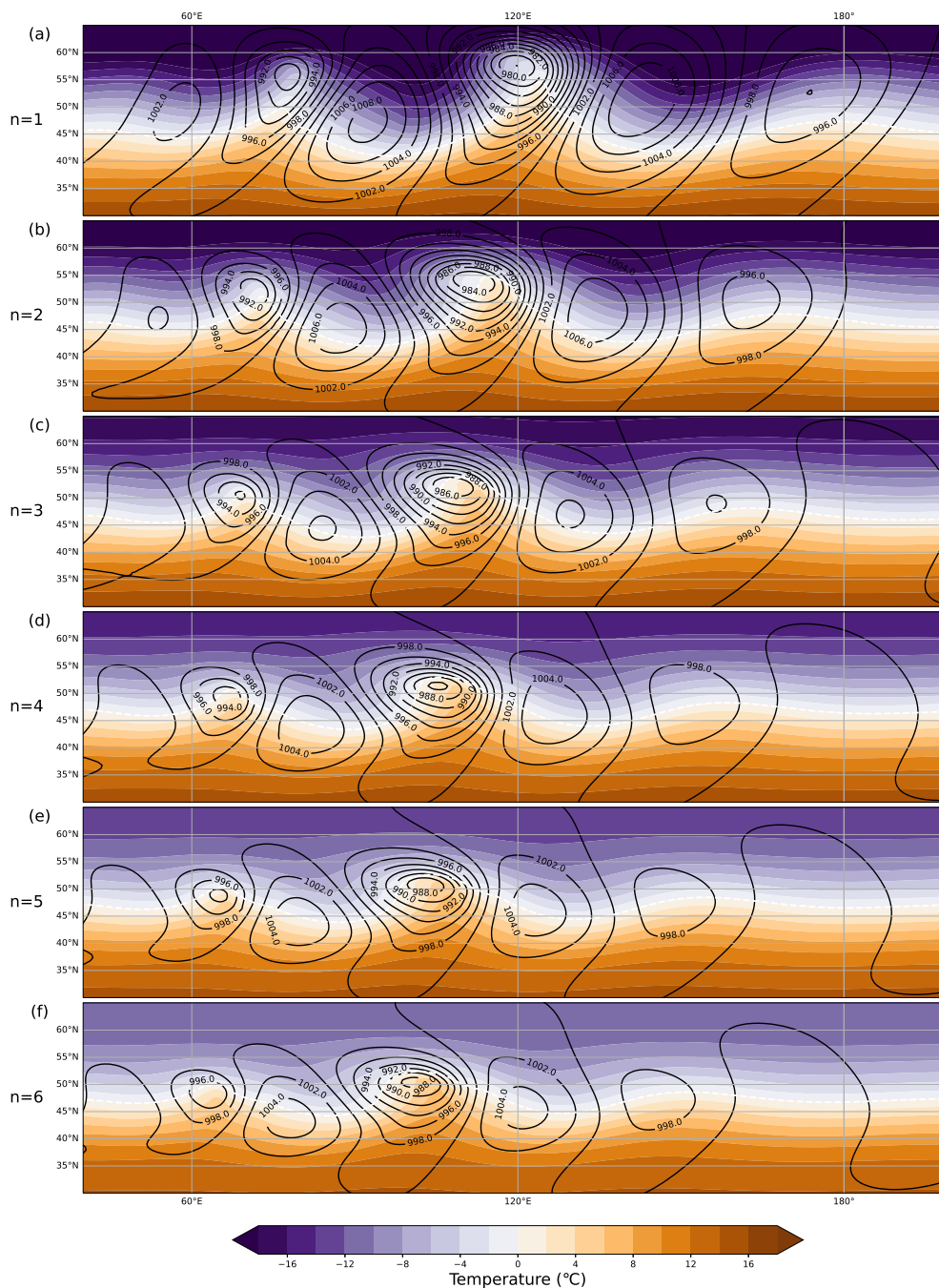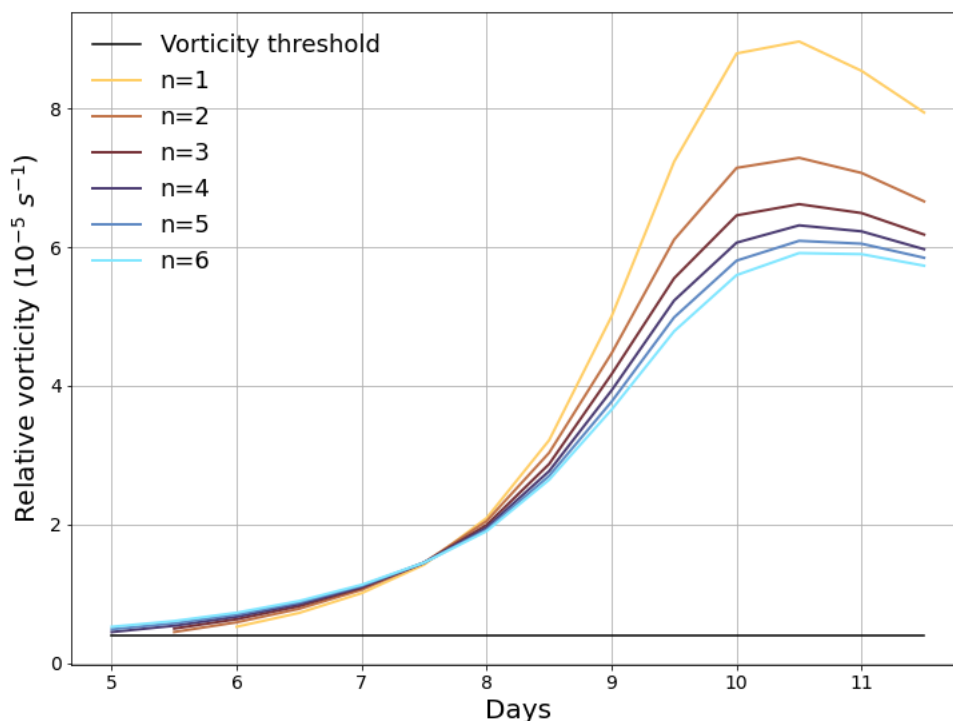
Figure 6. The development of the baroclinic wave at t=204h for (a) n=1, (b) n=2, (c) n=3, (d) n=4, (e) n=5, (f) n=6. The black contours show mean sea level pressure (hPa), the shading shows the temperature (°C) at the 850 hPa level. Note: this figure does not show the whole model domain; the x-axis ranges from 40-220°E, while the y-axis ranges from 30-65°N.

Figure 7. Evolution of the maximum relative vorticity of the first cyclone to develop as part of the baroclinic wave as a function of time. The black horizontal line shows the threshold for relative vorticity set to $0.4\ 10^{-5}\mathrm{s}^{-1}$ used by the tracking algorithm TRACK.

6 Conclusions

This article introduced an idealised initial background state for a baroclinic lifecycle simulation. The main advantages of these background states are that they can entirely be expressed analytically and controlled through configuration files. The jet structure and strength can be tuned as well as the average virtual temperature, the surface relative humidity, the lapse rate and the surface roughness. This flexibility allows an easy generation of different background states and their related baroclinic waves. All studied initial background states are proven to be stable even in the moist case scenario. Moreover, a Gaussian perturbation of the zonal wind speed allow the development of a baroclinic wave, which depends on the given jet structure. The presented solution is appealing for two main reasons.

First, the proposed solution is implemented in OpenIFS cycle 43r3, which is a popular state-of-the-art model used extensively for meteorological and climate research (Carver, 2021). The idea was to propose a solution easy to test and use to allow a wide accessibility. Moreover, the Appendix presents the exhaustive integration and derivation of the initial background state to allow

21

easy modification of the analytical formulae of the zonal wind speed field and the easy identification of the potential difficulties of its integration. One limitation of our initial state is that in its current form it is not possible to easily add barotropic shear

425 to the low-level of the jet. Barotropic shear has been proven to be a defining condition for the structure development of the extra-tropical cyclones (Agustí-Panareda et al., 2005). Future work will address this issue by proposing an analytical solution including an analytical barotropic shear.

Second, the initial background states are proven to be unstable to moist saturated air parcel displacements. The initial background states are proven to be realistic considering ERA5 average temperature and zonal wind speed cross-sections.

430 Moreover, this study have proven the sensitivity of the BWS to the height and width of the jet, which has been possible by the control of the different parameter through OpenIFS namelist. The proposed solution is of interest to create a large ensemble of baroclinic lifecycles which would allow the study of the sensitivity of ETC to various initial background states. Future study will investigate the dependency of several measure of cyclone's intensities - such as mean sea level pressure, relative vorticity at 850 hPa, 10-m wind gust and SSI (Leckebusch et al., 2008) - to the initial conditions of cyclogenesis.

Appendix A: Detailed Derivation of Analytical Initial Conditions

The derivation of the analytical initial conditions start from the primitive equations for moist adiabitic and frictionless flow in
440 spherical coordinates (λ, ϕ) and vertical $\eta = p/p_s$ levels by the equations for

$$\text{u-momentum: } \frac{du}{dt} - \frac{uv \tan\phi}{a} = -\frac{1}{a\cos\phi}\left(\frac{\partial\Phi}{\partial\lambda} + R_d T_v \frac{\partial\ln p}{\partial\lambda}\right) + fv \tag{A1a}$$

$$\text{v-momentum: } \frac{dv}{dt} + \frac{u^2 \tan\phi}{a} = -\frac{1}{a}\left(\frac{\partial\Phi}{\partial\phi} + R_d T_v \frac{\partial\ln p}{\partial\lambda}\right) - fu \tag{A1b}$$

$$\text{hydrostatic balance: } \frac{\partial\Phi}{\partial\eta} = -\frac{R_d T_v}{p}\frac{\partial p}{\partial\eta} \tag{A1c}$$

$$\text{continuity: } \frac{\partial}{\partial t}\left(\frac{\partial p}{\partial\eta}\right) + \frac{1}{a\cos\phi}\frac{\partial}{\partial}\left(u\frac{\partial p}{\partial\eta}\right) + \frac{1}{a\cos\phi}\frac{\partial}{\partial\phi}\left((v\cos\phi)\frac{\partial p}{\partial\eta}\right) + \frac{\partial}{\partial\eta}\left(\dot\eta\frac{\partial p}{\partial\eta}\right) = 0, \tag{A1d}$$

445 $$\text{thermodynamic: } \frac{dT}{dt} - \frac{R_d T_v \omega}{c_p p} = 0, \text{ and} \tag{A1e}$$

$$\text{moist ideal gas law: } p = \rho R_d T_v, \tag{A1f}$$

where d/dt is the full time derivative in spherical coordinates given as

$$\frac{d}{dt}() = \frac{\partial}{\partial t} + \frac{u}{a\cos\theta}\frac{\partial}{\partial\lambda}() + \frac{v}{a}\frac{\partial}{\partial\phi}() + \dot\eta\frac{\partial}{\partial\eta}().$$

Please not that the specific heat capacity of air, c_p, in the thermodynamic equation needs to be corrected with a correction factor when moisture is included in the model.

The following equalities are used in the derivations of the geopotential field

$$* \sin(2\phi) = 2\sin\phi\cos\phi$$

$$** \sin^2\phi = 1 - \cos^2\phi$$

$$*** (a+b)^n = \sum_{k=0}^{n} \binom{n}{k} a^{n-k} b^k$$

$$+ \tan\phi = \frac{\sin\phi}{\cos\phi}$$

$$\dagger \int_{-\pi/2}^{\pi/2} \cos^{2(k+n+1)}\phi \, d\phi = \sqrt{\pi}\frac{\Gamma(k+n+3/2)}{\Gamma(k+n+2)} \text{ , see e.g. WolframAlpha}$$

$$\ddagger \int_{-\pi/2}^{\pi/2} \sin^{2(k+2n+1)}\phi\cos\phi \, d\phi = \int_{-1}^{1} u^{2(k+2n+1)} du = \frac{2}{2(2n+k+1)+1}.$$

Whenever an equality is used its symbol is noted above the equality sign, for example $\overset{*}{=}$.

A1 Mean Geopotential Field

The mean virtual temperature field is defined as

$$\langle T_v \rangle = T_{v,0} - \gamma z, \tag{A2}$$

where $T_{v,0}$ is the reference virtual temperature, γ the lapse rate, and z height (moist version of (Eq. (10), Ullrich et al., 2015)). The geopotential mean field is derived from the mean virtual temperature field and the hydrostatic balance eqauation as follows

$$\frac{\partial p}{\partial z} = -\rho g$$

$$\frac{\partial p}{\partial z} = -\frac{p}{R_d\langle T_v\rangle}\bigg| \text{ Eq. (A2)}$$

$$\frac{\partial p}{p} = -\frac{g}{R_d(T_{v,0-\gamma z}}\partial z\bigg| \text{ integrate LH and RH}$$

$$\int_{p_s}^{p} \frac{\partial p}{p} = -\frac{g}{R_d}\int_{z_0=0}^{z} \frac{1}{(T_{v,0}-\gamma z)}\partial z. \tag{A3}$$

The left-hand side of Eq. (A3) is solved as

$$\int_{p_s}^{p} \frac{\partial p}{p} = \ln\frac{p}{p_s}, \tag{A4}$$

470   and the right-hand side of Eq. (A3) is solved by substitution of $u = T_{v,0} - \gamma z$. The right-hand side is solved as

$$-\frac{g}{R_d} \int\limits_{z=0}^{z} \frac{1}{(T_{v,0} - \gamma z)} \partial z = \frac{g}{R_d \gamma} \ln \frac{Tv, 0 - \gamma z}{T_{v,0}}. \tag{A5}$$

By solving for z, this gives us that

$$z = \frac{T_{v,0}}{\gamma} \left[1 - \left(\frac{p}{p_0} \right)^{\frac{R_d g}{\gamma}} \right], \tag{A6}$$

and by realising that p/p_s is η, the mean geopotential field is then

475   $$\langle \Phi \rangle = \frac{g T_{v,0}}{\gamma} \left(1 - \eta^{\frac{R_d g}{\gamma}} \right). \tag{A7}$$

A2   Geopotential Field

The geopotential anoamly field is derived from the steady-state momentum equation for v with the zonal flow defined by $u = -u_0 \ln \eta \exp(-[\ln \eta / b]^2) \sin^{2n} 2\phi$

$$\frac{1}{a} \frac{\partial \Phi'}{\partial \phi} = -(-u_\eta \sin^{2n} 2\phi) \left(2\Omega \sin \phi + \frac{-u_\eta \sin^{2n} 2\phi}{a} \tan \phi \right), \tag{A8}$$

480   where $u_\eta = u_0 \ln \eta \exp(-[\ln \eta / b]^2)$. Equation (A8) is multiplied by a and then integrated analytically over ϕ

$$\Phi'(\lambda, \phi, \eta) = \int \left[u_\eta \sin^{2n} 2\phi (2a\Omega \sin \phi - u_\eta \sin^{2n} 2\phi \tan \phi) \right] d\phi + \Phi_0(\eta), \tag{A9}$$

which is solved by dividing the integral into two parts that are solved separately

$$\int u_\eta \sin^{2n} 2\phi \, 2a\Omega \sin \phi \, d\phi = u_\eta 2a\Omega \int \sin^{2n} 2\phi \sin \phi \, d\phi \tag{A10a}$$

$$\int -u_\eta^2 \sin^{2n} 2\phi \sin^{2n} 2\phi \tan \phi \, d\pi = -u_\eta^2 \int \sin^{4n} 2\phi \tan \phi \, d\phi. \tag{A10b}$$

485   Eq. (A10a) is solved

$$\int \sin^{2n}(2\phi) \sin \phi \, d\phi \overset{*}{=} \int (2 \sin \phi \cos \phi)^{2n} \sin \phi \, d\phi$$

$$= 2^{2n} \int \sin^{2n} \phi \cos^{2n} \phi \sin \phi \, d\phi$$

$$\overset{**}{=} 4^n \int (1 - \cos^2 \phi)^n \cos^{2n} \phi \sin \phi \, d\phi,$$

24

which is integrated by substituting $u = \cos\phi$ and $du = -\sin\phi$

490

$$4^n \int (1 - \cos^2\phi)^n \cos^{2n}\phi \sin\phi d\phi = -4^n \int (1 - u^2)^n u^{2n} du$$

$$\stackrel{***}{=} -4^n \int \left(\sum_{k=0}^{n} \binom{n}{k} (-1)^k u^{2(k+n)} \right) du$$

$$= -4^n \sum_{k=0}^{n} \binom{n}{k} (-1)^k \int u^{2(k+n)} du$$

$$= -4^n \sum_{k=0}^{n} \binom{n}{k} (-1)^k \frac{1}{2(k+n)+1} u^{2(k+n)+1}$$

$$= -4^n \sum_{k=0}^{n} \binom{n}{k} (-1)^k \frac{1}{2(k+n)+1} \cos^{2(k+n)+1}\phi.$$

495   Hence,

$$\int u_\eta \sin^{2n} 2\phi 2a\Omega \sin\phi d\phi = -u_\eta 2a\Omega 4^n \sum_{k=0}^{n} \binom{n}{k} (-1)^k \frac{1}{2(k+n)+1} \cos^{2(k+n)+1}\phi. \tag{A11}$$

Then, Eq. (A10b) is solved

$$\int \sin^{4n}(2\phi) \tan\phi d\phi \stackrel{+,*}{=} \int (2\sin\phi\cos\phi)^{4n} \frac{\sin\phi}{\cos\phi} d\phi$$

$$= 2^{4n} \int \sin^{4n+1}\phi \cos^{4n-1}\phi d\phi$$

500

$$= 16^n \int \sin^{4n+1}\phi \cos^{2(2n-1)}\phi) \cos\phi d\phi$$

$$\stackrel{**}{=} 16^n \int \sin^{4n+1}\phi (1 - \sin^2\phi)^{2n-1} \cos\phi d\phi,$$

which is integrated by substituting $u = \sin\phi$ and $du = \cos\phi$. That gives us

$$16^n \int \sin^{4n+1}\phi (1 - \sin^2\phi)^{2n-1} \cos\phi d\phi = 16^n \int u^{4n+1}(1 - u^2)^{2n-1} du$$

$$\stackrel{***}{=} 16^n \int \left(u^{4n+1} \sum_{k=0}^{2n-1} \binom{2n-1}{k} (-1)^k u^{2k} \right) du$$

505

$$= 16^n \int \left(\sum_{k=0}^{2n-1} \binom{2n-1}{k} (-1)^k u^{2k+4n+1} \right) du$$

$$= 16^n \sum_{k=0}^{2n-1} \binom{2n-1}{k} (-1)^k \int \left(u^{2k+4n+1} \right) du$$

$$= 16^n \sum_{k=0}^{2n-1} \binom{2n-1}{k} (-1)^k \frac{1}{2(k+2n+1)} u^{2(k+2n+1)}$$

$$= 16^n \sum_{k=0}^{2n-1} \binom{2n-1}{k} (-1)^k \frac{1}{2(k+2n+1)} \sin^{2(k+2n+1)} 2\phi.$$

25

Hence,

$$510 \quad -u_\eta^2 \int \sin^{4n} 2\phi \tan\phi d\phi = -u_\eta^2 16^n \sum_{k=0}^{2n-1} \binom{2n-1}{k}(-1)^k \frac{1}{2(k+2n+1)} \sin^{2(k+2n+1)} 2\phi. \tag{A12}$$

Combining the solutions of Eqs. (A10a) and (A10b) gives us the solution for Φ'

$$\Phi'(\lambda,\phi,\eta) = -u_\eta 2a\Omega 4^n \sum_{k=0}^{n} \binom{n}{k}(-1)^k \frac{1}{2(k+n)+1} \cos^{2(k+n)+1}\phi \tag{A13}$$

$$-u_\eta^2 16^n \sum_{k=0}^{2n-1} \binom{2n-1}{k}(-1)^k \frac{1}{2(k+2n+1)} \sin^{2(k+2n+1)} 2\phi$$

$$+ \Phi_0(\eta).$$

Since the deviations of Φ' vanishes when averaging horizontally, we solve for Φ_0 by solving the equation

$$\frac{1}{4\pi} \int_0^{2\pi} \int_{-\pi/2}^{\pi/2} \Phi'(\lambda,\phi,\eta) \cos\phi d\phi d\lambda = 0 \tag{A14}$$

by inserting the expression for $\Phi'(\lambda,\phi,\eta)$

$$\frac{1}{4\pi} \int_0^{2\pi} \int_{-\pi/2}^{\pi/2} [-u_\eta 2a\Omega 4^n \sum_{k=0}^{n} \binom{n}{k}(-1)^k \frac{1}{2(k+n)+1} \cos^{2(k+n)+1}\phi \tag{A15}$$

$$-u_\eta^2 16^n \sum_{k=0}^{2n-1} \binom{2n-1}{k}(-1)^k \frac{1}{2(k+2n+1)} \sin^{2(k+2n+1)} 2\phi$$

$$520 \quad + \Phi_0(\eta)] \cos\phi d\phi d\lambda = 0.$$

Equation (A15) is divided into three parts

$$\frac{1}{4\pi} \int_0^{2\pi} \int_{-\pi/2}^{\pi/2} \left(-u_\eta 2a\Omega 4^n \sum_{k=0}^{n} \binom{n}{k}(-1)^k \frac{1}{2(k+n)+1} \cos^{2(k+n)+1}\phi\right) \cos\phi d\phi d\lambda \tag{A16a}$$

$$\frac{1}{4\pi} \int_0^{2\pi} \int_{-\pi/2}^{\pi/2} \left(-u_\eta^2 16^n \sum_{k=0}^{2n-1} \binom{2n-1}{k}(-1)^k \frac{1}{2(k+2n+1)} \sin^{2(k+2n+1)}\phi\right) \cos\phi d\phi d\lambda \tag{A16b}$$

$$\frac{1}{4\pi} \int_0^{2\pi} \int_{-\pi/2}^{\pi/2} \Phi_0(\eta) \cos\phi d\phi d\lambda. \tag{A16c}$$

525 The first part, Eq. (A16a), is solved as follows

$$
\frac{1}{4\pi}\int\limits_{0}^{2\pi}\int\limits_{-\pi/2}^{\pi/2}\left(-u_\eta 2a\Omega 4^n \sum_{k=0}^{n}\binom{n}{k}(-1)^k\frac{1}{2(k+n)+1}\cos^{2(k+n)+1}\phi\right)\cos\phi\, d\phi\, d\lambda
$$

$$
=-u_\eta 2a\Omega 4^n\frac{1}{4\pi}\int\limits_{0}^{2\pi}\int\limits_{-\pi/2}^{\pi/2}\left(\sum_{k=0}^{n}\binom{n}{k}(-1)^k\frac{1}{2(k+n)+1}\cos^{2(k+n+1)}\phi\right)d\phi\, d\lambda
$$

$$
=-u_\eta 2a\Omega 4^n\frac{1}{4\pi}\int\limits_{0}^{2\pi}\left(\sum_{k=0}^{n}\binom{n}{k}(-1)^k\frac{1}{2(k+n)+1}\int\limits_{-\pi/2}^{\pi/2}\cos^{2(k+n+1)}\phi\, d\phi\right)d\lambda
$$

$$
\overset{\ddagger}{=}-u_\eta 2a\Omega 4^n\frac{1}{4\pi}\int\limits_{0}^{2\pi}\left(\sum_{k=0}^{n}\binom{n}{k}(-1)^k\frac{1}{2(k+n)+1}\sqrt{\pi}\frac{\Gamma(k+n+3/2)}{\Gamma(k+n+2)}\right)d\lambda
$$

530
$$
=-u_\eta 2a\Omega 4^n\frac{1}{4\pi}2\pi\left(\sum_{k=0}^{n}\binom{n}{k}(-1)^k\frac{1}{2(k+n)+1}\sqrt{\pi}\frac{\Gamma(k+n+3/2)}{\Gamma(k+n+2)}\right)
$$

$$
=-u_\eta a\Omega 4^n\left(\sum_{k=0}^{n}\binom{n}{k}(-1)^k\frac{1}{2(k+n)+1}\sqrt{\pi}\frac{\Gamma(k+n+3/2)}{\Gamma(k+n+2)}\right),
$$

where $\Gamma(z)$ is the Gamma function. The second part, Eq. (A16b), is integrated by substituting $u=\sin\phi$ and $du=\cos\phi$ as
follows

$$
\frac{1}{4\pi}\int\limits_{0}^{2\pi}\int\limits_{-\pi/2}^{\pi/2}\left(u_\eta^2 16^n\sum_{k=0}^{2n-1}\binom{2n-1}{k}(-1)^k\frac{1}{2(k+2n+1)}\sin^{2(k+2n+1)}\phi\right)\cos\phi\, d\phi\, d\lambda
$$

535
$$
=-u_\eta^2 16^n\frac{1}{4\pi}\int\limits_{0}^{2\pi}\left(\sum_{k=0}^{2n-1}\binom{2n-1}{k}(-1)^k\frac{1}{2(k+2n+1)}\int\limits_{-\pi/2}^{\pi/2}\sin^{2(k+2n+1)}\phi\cos\phi\, d\phi\right)d\lambda
$$

$$
\overset{\ddagger}{=}-u_\eta^2 16^n\frac{1}{4\pi}\int\limits_{0}^{2\pi}\left(\sum_{k=0}^{2n-1}\binom{2n-1}{k}(-1)^k\frac{1}{2(k+2n+1)}\frac{2}{2(2n+k+1)+1}\right)d\lambda
$$

$$
=-u_\eta^2 16^n\frac{1}{4\pi}2\pi\sum_{k=0}^{2n-1}\binom{2n-1}{k}(-1)^k\frac{1}{2(k+2n+1)}\frac{2}{2(2n+k+1)+1}
$$

$$
=-u_\eta^2\frac{16^n}{2}\sum_{k=0}^{2n-1}\binom{2n-1}{k}(-1)^k\frac{1}{2(2n+k+1)}\frac{2}{2(2n+k+1)+1}
$$

The third part, Eq. (A16c), is solved as

540
$$
\frac{1}{4\pi}\int\limits_{0}^{2\pi}\int\limits_{-\pi/2}^{\pi/2}\Phi_0(\eta)\cos\phi\, d\phi\, d\lambda=\Phi_0(\eta),
$$

27

which gives us that

$$
\Phi_0(\eta) = -\big((\text{A16a}) + (\text{A16b})\big)
$$

$$
= -\Bigg(-u_\eta a \Omega 4^n \sum_{k=0}^{n} \binom{n}{k}(-1)^k \frac{1}{2(k+n)+1} \sqrt{\pi}\frac{\Gamma(k+n+3/2)}{\Gamma(k+n+2)}
$$

$$
- u_\eta^2 \frac{16^n}{2} \sum_{k=0}^{2n-1} \binom{2n-1}{k}(-1)^k \frac{1}{2(2n+k+1)} \frac{2}{2(2n+k+1)+1} \Bigg)
$$

$$
= u_\eta a \Omega 4^n \sum_{k=0}^{n} \binom{n}{k}(-1)^k \frac{1}{2(k+n)+1} \sqrt{\pi}\frac{\Gamma(k+n+3/2)}{\Gamma(k+n+2)}
$$

$$
+ u_\eta^2 \frac{16^n}{2} \sum_{k=0}^{2n-1} \binom{2n-1}{k}(-1)^k \frac{1}{2(2n+k+1)} \frac{2}{2(2n+k+1)+1}. \tag{A17}
$$

Combining Eqs. (A13) and (A17) leads us to the final expression for the deviation of the geopotential field

$$
\Phi'(\lambda,\phi,\eta) = u_\eta a \Omega 4^n \Bigg(\underbrace{\sum_{k=0}^{n} \binom{n}{k}(-1)^k \frac{1}{2(k+n)+1} \sqrt{\pi}\frac{\Gamma(k+n+3/2)}{\Gamma(k+n+2)}}_{:=F_3}
$$

$$
-2 \underbrace{\sum_{k=0}^{n} \binom{n}{k}(-1)^k \frac{1}{2(k+n)+1} \cos^{2(k+n)+1}\phi}_{:=F_1} \Bigg)
$$

$$
+ u_\eta^2 16^n \Bigg(\frac{1}{2} \underbrace{\sum_{k=0}^{2n-1} \binom{2n-1}{k}(-1)^k \frac{1}{2(2n+k+1)} \frac{2}{2(2n+k+1)+1}}_{:=F_4}
$$

$$
- \underbrace{\sum_{k=0}^{2n-1} \binom{2n-1}{k}(-1)^k \frac{1}{2(k+2n+1)} \sin^{2(k+2n+1)}2\phi}_{:=F_2} \Bigg).
$$

It can be re-write as

$$
\Phi'(\lambda,\phi,\eta) = u_\eta a \Omega 4^n \Big(F_3 - 2F_1 \Big) + u_\eta^2 16^n \Big(\frac{1}{2}F_4 - F_2 \Big), \tag{A18}
$$

where

$$F_1 = \sum_{k=0}^{n} \binom{n}{k} (-1)^k \frac{1}{2(k+n)+1} \cos^{2(k+n)+1} \phi \tag{A19a}$$

$$F_2 = \sum_{k=0}^{2n-1} \binom{2n-1}{k} (-1)^k \frac{1}{2(k+2n)+1} \sin^{2(k+2n+1)} 2\phi \tag{A19b}$$

$$F_3 = \sum_{k=0}^{n} \binom{n}{k} (-1)^k \frac{1}{2(k+n)+1} \sqrt{\pi} \frac{\Gamma(k+n+3/2)}{\Gamma(k+n+2)} \tag{A19c}$$

$$F_4 = \sum_{k=0}^{2n-1} \binom{2n-1}{k} (-1)^k \frac{1}{2(2n+k+1)} \frac{2}{2(2n+k+1)+1} \tag{A19d}$$

$$u_\eta = u_0 \ln \eta \exp(-[\ln \eta / b]^2). \tag{A19e}$$

The geopotential field is now described as

$$\Phi(\lambda, \phi, \eta) = \langle \Phi(\eta) \rangle + \Phi'(\lambda, \phi, \eta) \tag{A20}$$

$$= \frac{T_{v,0} g}{\gamma} (1 - \eta^{\frac{R_d \gamma}{g}}) + \Phi'(\lambda, \phi, \eta), \tag{A21}$$

where the expression for $\langle \Phi(\eta) \rangle$ is the expression derived in Sec. A1 and the same as (Eq. (7), Ullrich et al., 2015).

A3 Virtual Temperature Field

We now have an expression for $\Phi'(\lambda, \phi, \eta)$ and we continue by deriving the virtual temperature anomaly field T' by starting from the hydrostatic balance

$$T_v'(\lambda, \phi, \eta) = -\frac{\eta}{R_d} \frac{\partial \Phi'(\lambda, \phi, \eta)}{\partial \eta}. \tag{A22}$$

We start by inserting the expression for Φ' Eq. (A18) and u_η into Eq. (A22) and then take the derivative with respect to η

$$T_v'(\lambda, \phi, \eta) = -\frac{\eta}{R_d} \frac{\partial}{\partial \eta} \left[u_\eta \underbrace{a\Omega 4^n (F_3 - 2F_1)}_{A_1} + u_\eta^2 \underbrace{16^n (\frac{1}{2} F_4 - F_2)}_{A_2} \right]$$

$$= -\frac{\eta}{R_d} \left[\frac{\partial u_\eta}{\partial \eta} A_1 + 2 \frac{\partial u_\eta}{\partial \eta} A_2 \right]$$

$$= -\frac{\eta}{R_d} \left[\frac{\partial u_\eta}{\partial \eta} (A_1 + 2A_2) \right].$$

As the terms F_1, F_2, F_3, F_4 do not depend on η, we only need to calculate

$$\frac{\partial u_\eta}{\partial \eta} = \frac{\partial}{\partial \eta} (u_0 \ln \eta \exp(-[\ln \eta / b]^2)) = u_0 \left[\frac{1}{\eta} \exp(-[\ln \eta / b]^2) + \ln \eta \exp(-[\ln \eta / b]^2) \frac{-2}{b^2} \ln \eta \frac{1}{\eta} \right]$$

$$= u_0 \frac{1}{\eta} \exp(-[\ln \eta / b]^2) \left(1 - \frac{2(\ln \eta)^2}{b^2} \right). \tag{A23}$$

575 Inserting Eq. (A23) into Eq. (A22) gives us that

$$T_v'(\lambda,\phi,\eta) = \frac{u_0}{R_d}\exp(-[\ln\eta/b]^2)\left(\frac{2(\ln\eta)^2}{b^2}-1\right)\left[a\Omega 4^n\left(F_3-2F_1\right)+16^n u_\eta\left(F_4-2F_2\right)\right]. \tag{A24}$$

The virtual temperature field is now described by

$$T_v(\lambda,\phi,\eta) = \langle T_v(\eta)\rangle + T_v'(\lambda,\phi,\eta) \tag{A25}$$

$$= T_{v,0}\eta^{\frac{R_d\gamma}{g}} + \frac{u_0}{R_d}\exp(-[\ln\eta/b]^2)\left(\frac{2(\ln\eta)^2}{b^2}-1\right)\left[a\Omega 4^n\left(F_3-2F_1\right)+16^n u_\eta\left(F_4-2F_2\right)\right], \tag{A26}$$

580 where $\langle T_v(\eta)\rangle$ is the moist version of (Eq. (10), Ullrich et al., 2015).

Competing interests. The contact author has declared that none of the authors has any competing interests.

References

Adamson, D. S., Belcher, S. E., Hoskins, B. J., and Plant, R. S. (2006). Boundary-layer friction in midlatitude cyclones. *QJ*, 132(614):101–124.

595   Agustí-Panareda, A., Gray, S. L., Craig, G. C., and Thorncroft, C. (2005). The extratropical transition of tropical cyclone lili (1996) and its crucial contribution to a moderate extratropical development. *MON WEATHER REV*, 133(6):1562–1573.

Beare, R. J. (2007). Boundary layer mechanisms in extratropical cyclones. *QJ*, 133(623):503–515.

Beljaars, A. C. (1995). The parametrization of surface fluxes in large-scale models under free convection. *QJ*, 121(522):255–270.

Carver, G. (2021). Ten years of openifs at ecmwf.

600   Charney, J. G. (1947). The dynamics of long waves in a baroclinic westerly current. *JAS*, 4(5):136–162.

Charnock, H. (1955). Wind stress on a water surface. *QJ*, 81(350):639–640.

Courtier, P. and Naughton, M. (1994). A pole problem in the reduced gaussian grid. *QJ*, 120(519):1389–1407.

Eady, E. T. (1949). Long waves and cyclone waves. *TELLUS*, 1(3):33–52.

ECMWF (2017a). *IFS Documentation CY43R3 - Part III: Dynamics and numerical procedures*. Number 3. ECMWF.

605   ECMWF (2017b). *IFS Documentation CY43R3 - Part IV: Physical processes*. Number 4. ECMWF.

Feldstein, S. B. and Held, I. M. (1989). Barotropic decay of baroclinic waves in a two-layer beta-plane model. *JAS*, 46(22):3416–3430.

Gamage, S. M., Sica, R., Martucci, G., and Haefele, A. (2020). A 1d var retrieval of relative humidity using the era5 dataset for the assimilation of raman lidar measurements. *J ATMOS OCEAN TECH*, 37(11):2051–2064.

Heckley, W. and Hoskins, B. (1982). Baroclinic waves and frontogenesis in a non-uniform potential vorticity semi-geostrophic model. *JAS*, 610   39(9):1999–2016.

Held, I. M. (1982). On the height of the tropopause and the static stability of the troposphere. *J ATMOS SCI*, 39(2):412–417.

Hersbach, H., Bell, B., Berrisford, P., Hirahara, S., Horányi, A., Muñoz-Sabater, J., Nicolas, J., Peubey, C., Radu, R., Schepers, D., et al. (2020). The era5 global reanalysis. *QJ*, 146(730):1999–2049.

Hines, K. M. and Mechoso, C. R. (1993). Influence of surface drag on the evolution of fronts. *MWR*, 121(4):1152–1176.

615   Hodges, K. (1995). Feature tracking on the unit sphere. *MON WEATHER REV*, 123(12):3458–3465.

Hodges, K. (1999). Adaptive constraints for feature tracking. *MON WEATHER REV*, 127(6):1362–1373.

Hodges, K. I. (1994). A general method for tracking analysis and its application to meteorological data. *MON WEATHER REV*, 122(11):2573–2586.

Holton, J. and Hakim, G. (2012). An introduction to dynamic meteorology.

620   Hoskins, B., Simmons, A., and Andrews, D. (1977). Energy dispersion in a barotropic atmosphere. *QJ*, 103(438):553–567.

Hoskins, B. J. and Simmons, A. J. (1975). A multi-layer spectral model and the semi-implicit method. *QJ*, 101(429):637–655.

Jablonowski, C. and Williamson, D. L. (2006). A baroclinic wave test case for dynamical cores of general circulation models: model intercomparisons. *NCAR/TN-4691STR*.

Khairoutdinov, M. F., Blossey, P. N., and Bretherton, C. S. (2022). Global system for atmospheric modeling: model description and prelimi-625   nary results. *J ADV MODEL EARTH SY*, 14(6):e2021MS002968.

Kirshbaum, D., Merlis, T., Gyakum, J., and McTaggart-Cowan, R. (2018). Sensitivity of idealized moist baroclinic waves to environmental temperature and moisture content. *JAS*, 75(1):337–360.

Kuo, Y.-H., Shapiro, M., and Donall, E. G. (1991). The interaction between baroclinic and diabatic processes in a numerical simulation of a rapidly intensifying extratropical marine cyclone. *MON WEATHER REV*, 119(2):368–384.

630 Langsdorf, S., Löschke, S., Möller, V., Okem, A., Officer, S., Rama, B., et al. (2022). Climate change 2022 impacts, adaptation and vulnerability working group ii contribution to the sixth assessment report of the intergovernmental panel on climate change.

Leckebusch, G. C., Renggli, D., and Ulbrich, U. (2008). Development and application of an objective storm severity measure for the northeast atlantic region. *METEOROL Z*, pages 575–587.

Lee, J. H., Kim, J.-H., Sharman, R. D., Kim, J., and Son, S.-W. (2023). Climatology of clear-air turbulence in upper troposphere and lower
635 stratosphere in the northern hemisphere using era5 reanalysis data. *J GEOPHYS RES-ATMOS*, 128(1):e2022JD037679.

Olson, J. B. and Colle, B. A. (2007). A modified approach to initialize an idealized extratropical cyclone within a mesoscale model. *MON WEATHER REV*, 135(4):1614–1624.

Park, C., Son, S.-W., and Kim, J.-H. (2021). Role of baroclinic trough in triggering vertical motion during summertime heavy rainfall events in korea. *J ATMOS SCI*, 78(5):1687–1702.

640 Polvani, L. M. and Esler, J. (2007). Transport and mixing of chemical air masses in idealized baroclinic life cycles. *J GEOPHYS RES-ATMOS*, 112(D23).

Purser, R. and Leslie, L. (1988). A semi-implicit, semi-lagrangian finite-difference scheme using hligh-order spatial differencing on a nonstaggered grid. *MON WEATHER REV*, 116(10):2069–2080.

Rantanen, M., Räisänen, J., Sinclair, V. A., and Järvinen, H. (2019). Sensitivity of idealised baroclinic waves to mean atmospheric temperature
645 and meridional temperature gradient changes. *CDYN*, 52(5-6):2703–2719.

Ritchie, H. and Beaudoin, C. (1994). Approximations and sensitivity experiments with a baroclinic semi-lagrangian spectral model. *MON WEATHER REV*, 122(10):2391–2399.

Romps, D. M. (2014). An analytical model for tropical relative humidity. *J CLIMATE*, 27(19):7432–7449.

Rupp, P. and Birner, T. (2021). Tropospheric eddy feedback to different stratospheric conditions in idealised baroclinic life cycles. *WCD*,
650 2(1):111–128.

Shapiro, M., Wernli, H., Bao, J.-W., Methven, J., Zou, X., Doyle, J., Holt, T., Donall-Grell, E., and Neiman, P. (1999). *The life cycles of extratropical cyclones*. Springer.

Simmons, A. J. and Hoskins, B. J. (1975). A comparison of spectral and finite-difference simulations of a growing baroclinic wave. *QJ*, 101(429):551–565.

655 Simmons, A. J. and Hoskins, B. J. (1978). The life cycles of some nonlinear baroclinic waves. *JAS*, 35(3):414–432.

Sinclair, V., Gray, S. L., and Belcher, S. E. (2010). Controls on boundary layer ventilation: Boundary layer processes and large-scale dynamics. *JGR*, 115(D11).

Sinclair, V. A. and Keyser, D. (2015). Force balances and dynamical regimes of numerically simulated cold fronts within the boundary layer. *QJ*, 141(691):2148–2164.

660 Stoelinga, M. T. (1996). A potential vorticity-based study of the role of diabatic heating and friction in a numerically simulated baroclinic cyclone. *MON WEATHER REV*, 124(5):849–874.

Tang, B. H., Fang, J., Bentley, A., Kilroy, G., Nakano, M., Park, M.-S., Rajasree, V., Wang, Z., Wing, A. A., and Wu, L. (2020). Recent advances in research on tropical cyclogenesis. *TCRR*, 9(2):87–105.

Terpstra, A. and Spengler, T. (2015). An initialization method for idealized channel simulations. *MWR*, 143(6):2043–2051.

665 Thorncroft, C. and Hoskins, B. (1990). Frontal cyclogenesis. *JAS*, 47(19):2317–2336.

Thorncroft, C., Hoskins, B., and McIntyre, M. (1993). Two paradigms of baroclinic-wave life-cycle behaviour. *QJ*, 119(509):17–55.

Tierney, G., Posselt, D. J., and Booth, J. F. (2018). An examination of extratropical cyclone response to changes in baroclinicity and temperature in an idealized environment. *CDYN*, pages 1–18.

Ullrich, P. and Jablonowski, C. (2012). Operator-split runge–kutta–rosenbrock methods for nonhydrostatic atmospheric models. *MWR*, 670   140(4):1257–1284.

Ullrich, P., Reed, K., and Jablonowski, C. (2015). Analytical initial conditions and an analysis of baroclinic instability waves in f-and β-plane 3d channel models. *QJ*, 141(693):2972–2988.

Wang, S. and Polvani, L. M. (2011). Double tropopause formation in idealized baroclinic life cycles: The key role of an initial tropopause inversion layer. *J GEOPHYS RES-ATMOS*, 116(D5).

675   Willison, J., Robinson, W. A., and Lackmann, G. M. (2013). The importance of resolving mesoscale latent heating in the north atlantic storm track. *J ATMOS SCI*, 70(7):2234–2250.

Yau, M. K. and Rogers, R. R. (1996). *A short course in cloud physics*. Elsevier.